Nonlinear registration of serial coronary CT angiography (CCTA) for assessment of changes in atherosclerotic plaque

Jonghye Woo
Departments of Imaging and Medicine, Cedars-Sinai Medical Center, Los Angeles, California 90048

Damini Dey
Departments of Imaging and Medicine, Cedars-Sinai Medical Center, Los Angeles, California 90048 and Department of Medicine, David-Geffen School of Medicine at UCLA, Los Angeles, California 90049

Victor Y. Cheng
Departments of Imaging and Medicine, Cedars-Sinai Medical Center, Los Angeles, California 90048

Byung-Woo Hong
School of Computer Science and Engineering, Chung-Ang University, Seoul, 156-756, Korea

Amit Ramesh
Departments of Imaging and Medicine, Cedars-Sinai Medical Center, Los Angeles, California 90048

Ganesh Sundaramoorthi
Computer Science, University of California, Los Angeles, California 90095

Ryo Nakazato
Departments of Imaging and Medicine, Cedars-Sinai Medical Center, Los Angeles, California 90048

Daniel S. Berman and Guido Germano
Departments of Imaging and Medicine, Cedars-Sinai Medical Center, Los Angeles, California 90048 and Department of Medicine, David-Geffen School of Medicine at UCLA, Los Angeles, California 90049

C.-C. Jay Kuo
Department of Electrical Engineering, University of Southern California, Los Angeles, California 90089-2564

Piotr J. Slomka[a)]
Departments of Imaging and Medicine, Cedars-Sinai Medical Center, Los Angeles, California 90048 and Department of Medicine, David-Geffen School of Medicine at UCLA, Los Angeles, California 90049

(Received 8 July 2009; revised 21 November 2009; accepted for publication 4 December 2009; published 28 January 2010)

Purpose: Coronary CT angiography (CCTA) is a high-resolution three-dimensional imaging technique for the evaluation of coronary arteries in suspected or confirmed coronary artery disease (CAD). Coregistration of serial CCTA scans would allow precise superimposition of images obtained at two different points in time, which could aid in recognition of subtle changes and precise monitoring of coronary plaque progression or regression. To this end, the authors aimed at developing a fully automatic nonlinear volume coregistration for longitudinal CCTA scan pairs.
Methods: The algorithm combines global displacement and local deformation using nonlinear volume coregistration with a volume-preserving constraint. Histogram matching of intensities between two serial scans is performed prior to nonlinear coregistration with dense nonparametric local deformation in which sum of squared differences is used as a similarity measure. The approximate segmentation of coronary arteries obtained from commercially available software provides initial anatomical landmarks for the coregistration algorithm that help localize and emphasize the structure of interest. To avoid possible bias caused by incorrect segmentation, the authors convolve the Gaussian kernel with the segmented binary coronary tree mask and define an extended weighted region of interest. A multiresolution approach is employed to represent coarse-to-fine details of both volumes and the energy function is optimized using a gradient descent method. The authors applied the algorithm in ten paired CCTA datasets (20 scans in total) obtained within 10.7 ± 5.7 months from each other on a dual source CT scanner to monitor progression of CAD.
Results: Serial CCTA coregistration was successful in 9/10 cases as visually confirmed. The global displacement and local deformation of target registration error obtained from four anatomical landmarks were 2.22 ± 1.15 and 1.56 ± 0.74 mm, respectively, and the inverse consistency error of local deformation was 0.14 ± 0.06 mm. The observer variability between two expert observers was 1.31 ± 0.91 mm.
Conclusions: The proposed coregistration algorithm demonstrates potential to accurately register serial CCTA scans, which may allow direct comparison of calcified and noncalcified atherosclerotic

plaque changes between the two scans. © *2010 American Association of Physicists in Medicine*.
[DOI: 10.1118/1.3284541]

Key words: nonlinear registration, serial coronary CT angiography, atherosclerotic plaque, plaque change

I. INTRODUCTION

Coronary artery disease (CAD) is a major cause of mortality in the industrial world. Coronary CT angiography (CCTA) has become an increasingly effective clinical tool for noninvasive assessment of the coronary arteries following the introduction of 64-slice CT scanners with fast gantry rotation times.[1,2] CCTA has demonstrated substantial potential for plaque detection, quantification, and characterization,[3,4] and for the assessment of positive coronary artery remodeling,[5] which is associated with unstable plaques. Recent studies have suggested that serial CCTA may be used to monitor untreated plaque progression over time[6] or assess plaque changes associated with lipid-lowering therapy.[7]

Currently, serial CCTA scans of the same patient, acquired at two separate times, are interpreted separately with individual multiplanar orientation and/or curvilinear displays.[8] This process is time consuming and it is difficult to ensure that the identical views of the artery are presented to the clinician in both scans. Imaging the coronory arteries with CT is challenging because of cardiac motion and the small diameter of coronary arteries (2–3 mm).[9] Furthermore, in visual comparison, it is not guaranteed that 2D images presented to the observer (either multiplanar reconstructions or curvilinear displays) refer to the same anatomical position. Due to the tortuous anatomy of the coronary vessels, even small differences in the image orientation and curvilinear image surface position may result in apparent changes in perceived plaque characteristics, introducing significant subjectivity. Recently, studies on manual plaque quantification of serial scans show that variability between different observers in measuring plaque volume and composition can be quite significant, especially in small plaques.[10,11] Accurate and automated coregistration of serial CCTA scans would ensure that multiplanar/curvilinear views depicting the same lesion on the two scans are presented in a common frame of reference. It would allow voxelwise comparison of coronary plaque composition, arterial stenosis, and remodeling at two time points, and potentially allow direct quantitative monitoring of plaque changes. However, coregistration of serial CCTA poses several challenges. First, there could be significant interscan intensity differences between the two scans due to data acquisition at two separate time points, with two contrast agent injections occurring at potentially different physiological states. Second, the algorithm must deform the source volume in the coronary artery region but preserve true plaque characteristics of source volume since there could be valid image changes due to the plaque development between the two scans.

These challenges motivate the use of algorithms that can leverage coregistration in conjunction with "anatomical features." Rigid registration is used to capture global displacement between source and target anatomical feature masks, which, however, is not sufficient to compensate for inherent cardiac and respiratory motion.[12] Subsequent nonlinear coregistration is applied to establish correspondence of the detailed deformation.

Nonlinear registration generally refers to the process of estimating the nonlinear mapping function which transforms each point in one image to a point in the target image. Common similarity measures include sum of squared differences (SSDs),[13] cross correlation (CC),[14] and information-theoretic measures such as mutual information (MI).[15] SSD and CC are well-suited when the source and target images have been acquired similarly, and thus have similar intensity range and distribution.[16] The MI measure has been adopted successfully for multimodal image coregistration without prior assumptions about the two images.[17] As for nonparametric dense registration methods, registration is inherently an ill-posed problem, and thus there is no unique solution. To compensate for the ill-posed nature of correspondence problems, several regularization techniques have been proposed. They include biharmonic,[18,19] diffusion,[20] and physical continuum models[21,22] such as linear elastic and viscous fluid regularizations. In addition to regularization techniques, there are also methods that impose constraints on the transformation such as inverse consistency,[23] volume preservation,[24,25] and topology preservation.[16]

Although the specific problem of serial CCTA image coregistration has not been addressed before, some related techniques have been proposed previously. Coregistration was proposed for measuring volume or shape changes in brain MRI scans;[26–29] in addition, related serial nonlinear CT coregistration techniques have been proposed for estimating interval changes for dose tracking, CT radiotherapy planning, and temporal subtraction of thoracic CT.[30–34] Nonetheless, CCTA application is uniquely demanding due to the high resolution of images, complex three-dimensional anatomy, potential for large changes between the two scans, and the requirement for high accuracy of registration to preserve the plaque characteristics after coregistration.

In this study, we propose a fully automatic serial coregistration method for CCTA scans using a dense nonparametric coregistration model by extending our preliminary approach, which combines segmentation of the vessels with image coregistration.[35] To mitigate the difficulties, the proposed method incorporates a binary "anatomical feature" obtained from segmentation of the arterial lumen, which is used within the registration method. To avoid possible bias caused by incorrect segmentation, we introduce a *soft* mask to consider the coronary artery and surrounding region; a volume-preserving constraint is also used to guarantee that the vol-

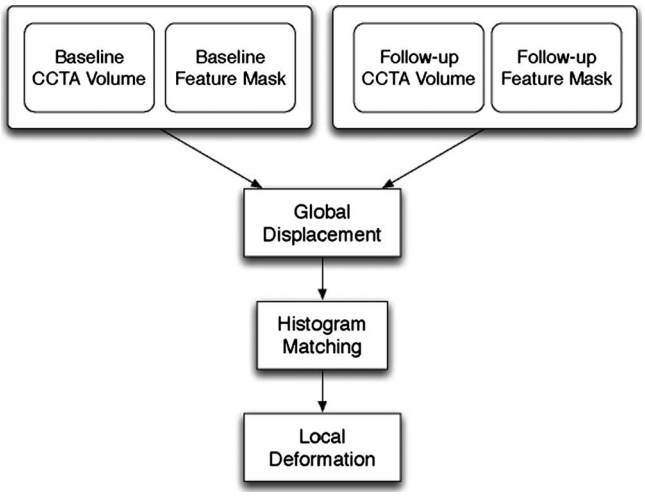

FIG. 1. Flowchart of the proposed method.

ume remains constant before and after the coregistration. Coregistration is a two-step procedure which consists of determining global displacement using binary feature masks, and subsequent local deformation within a variational framework. Prior to local deformation, histogram matching is performed to compensate for potential intensity differences, thus resulting in similar image characteristics between the two scans. The proposed approach incorporates combined information obtained from image intensities and geometrical features.

II. MATERIALS AND METHODS

II.A. Description of method

We classify the problem as the same modality and intrasubject coregistration since serial CCTA scans are obtained from the same patient at different time instances. The goal of our serial coregistration is to estimate the transformation that aligns coronary arteries in 3D, thereby allowing assessment of the regression and progression of coronary plaques in the arteries. To summarize, our coregistration scheme consists of two sequential steps: (1) A rigid coregistration scheme for global displacement based on a presegmented binary mask, and (2) a final nonlinear coregistration that accounts for local vessel deformation after histogram matching of intensity distribution in the two scans. Global displacement is initially obtained by the optimal rigid coregistration between the two presegmented binary masks, and the local deformation is subsequently obtained by optimal nonlinear coregistration, with a volume-preserving constraint. In the coregistration process, we utilize coronary trees that are initially obtained by the commercially available coronary artery segmentation software (Circulation, Syngo MMWP Version VE31A, Siemens Medical Solutions, Forchheim, Germany) and use them as initial anatomical feature masks. The flowchart of the proposed coregistration method is given in Fig. 1.

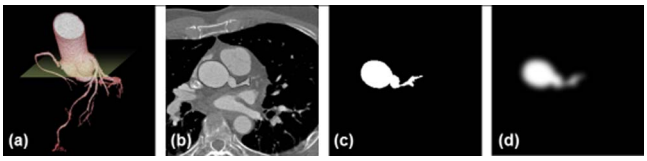

FIG. 2. Coronary tree mask used in image coregistration. (a) Presegmented 3D binary mask covers the coronary tree region. 3D mask is shown with a representative 2D slice. This representative slice from 3D image is overlaid with presegmented mask boundary (line) (b). The 2D presegmented binary mask for this slice is shown in (c), and the 2D soft mask for this slice generated by convolving with the Gaussian kernel is shown in (d). The 3D soft mask is created for the entire 3D coronary region.

II.A.1. Feature mask

We utilize binary coronary trees as initial feature masks. The binary 3D map containing voxels of the coronary arterial lumen may not be accurate and complete due to initial segmentation errors (missing portions, inclusion of noise and extra coronary structures), which could lead to subsequent bias in the coregistration process. However, it does provide a useful reference for the initial region of interest as long as plaques of interest are contained within. We utilize an expanded mask, generated by convolving the Gaussian kernel with the binary coronary tree mask (referred to as "soft mask"), to account for neighboring vessel region; this can be viewed as a Gaussian weighting function to emphasize the central area and weaken the bias of presegmented binary maps. Examples of the binary and soft mask are shown in Fig. 2.

Binary masks of coronary trees in target volume I and source volume J are $M_I, M_J: \Omega \rightarrow \Re^+$, respectively. They were obtained automatically with the CCTA segmentation software (Circulation, Syngo MMWP Version VE31A, Siemens Medical Solutions)[36] available on the Siemens Syngo workstation. The soft masks favor certain locations of domain $x \in \Omega$ for source and target volume and are given by

$$m_I = G_\sigma * M_I \quad \text{and} \quad m_J = G_\sigma * M_J, \tag{1}$$

where $*$ denotes the convolution operator and G_σ is a Gaussian kernel with standard deviation σ.

II.A.2. Global displacement model

The global displacement model is described by a rigid coregistration which includes rotation and translation (six degrees of freedom in 3D) to account for large displacements. Since the presegmented coronary tree regions are routinely and automatically obtained from CCTA scans during clinical analysis, we can use them for source and target shapes in the initial coregistration without reducing practicality of the approach. We employ explicit parameters to account for translation (by displacement parameter μ) and rotation (by angular parameter θ) from source image M_J to target image M_I, which are defined on the image domain Ω. The energy functional for the rigid transformation is given as

$$E_{\text{global}}(x,\mu,\theta)=\int_{\Omega}(M_I(x)-M_J(R_\theta x+\mu))^2dx. \quad (2)$$

Furthermore, we employ a coarse-to-fine multiresolution scheme for the computational efficiency and robustness. The optimal values for the six parameters that minimize the given energy functional are obtained by solving the associated Euler–Lagrange equations, and a gradient descent method is performed. This global displacement model is used to achieve the initial structural matching before the subsequent feature-based nonlinear volume coregistration.

II.A.3. Local deformation model

Rigid transformation captures only the global displacement of the coronary vessels between the two scans. Further local deformation is needed to achieve more accurate coregistration due to myocardial tissue deformations and residual cardiac phase differences.

The basic assumption of the proposed energy functional is similar to that of optical flow[37] in that it maintains the brightness constancy assumption in the two scans. To compensate for the potential intensity differences, contrast correction is performed using histogram matching technique, which normalizes the intensity values of a source volume based on the intensity values of a target volume. Additionally, to preserve the true morphology of plaque lesions in the process of serial coregistration, several constraints are imposed in the nonlinear coregistration process. First, we constrain the registration to the coronary artery region. Second, the total volume of the coronary vessels should be preserved in the transformation. We therefore exploit feature masks and obtain local displacements by an optimal nonlinear transformation with a volume-preserving constraint as detailed below. Finally, we constrain the solution by adding smoothness term to establish correspondences with spatial coherence even in the presence of potential plaque development.

Let I and J be the source and target volumes contained in Ω, which corresponds to an open and bounded domain in $\Re^n$. Without loss of generality, we consider the three-dimensional case. Coregistration between two volumes is equivalent to finding a smooth deformation defined on the image domain Ω,

$$h(x):\Omega\rightarrow\Omega, \quad (3)$$

where $h(x)$ denotes a 3D displacement vector at each voxel that allows infinite dimensional deformation. The optimal solution is found by minimizing an energy functional which consists of a data fidelity term that measures the similarity of source and target volume within the soft mask region and a smoothness term for volume matching as follows:

$$E=E_{\text{data}}+\alpha E_{\text{smooth}}, \quad (4)$$

where α is a weighting parameter.

The data fidelity term is defined as the sum of squared differences within the soft mask region

$$E_{\text{data}}=\int_{\Omega}m_I(x)|I(x)-J\circ h(x)|^2dx. \quad (5)$$

We can emphasize the coronary tree region using the soft mask as a weighting function that restricts the domain of the similarity measure.

Recovering the optimal deformation of this objective function is not straightforward. Due to the lack of information, the complete recovery of the local deformation field is an ill-posed problem. The use of regularization is a common practice to overcome this limitation,[20] with smoothness of the pixelwise motion field as a natural coregistration assumption.

The regularization term penalizes large variations in the transformation to ensure that displacement $h(x)$ is continuous. We adopt the diffusion regularization[20] that penalizes the total variation of the flow field, which can be expressed as

$$E_{\text{smooth}}=\int_{\Omega}|\nabla h(x)|^2dx. \quad (6)$$

Now the objective is to find the optimal deformation $h(x)$ that minimizes this energy functional while preserving the volume.

We use the soft mask as a weighting function, which provides a mechanism to include the local neighborhood of regions of interest in the coregistration process. In our coregistration scheme, we applied Gaussian kernel with standard deviation σ (e.g., 10 pixels) to include neighboring region and to weaken the bias caused by the segmentation algorithm.

II.A.4. Constrained volume-preserving flow

Nonlinear coregistration can potentially change the original volume of structures, which in our case is highly undesirable. As stated before, the volume-preservation constraint is necessary to monitor changes in the target plaque region. The idea of using the Jacobian determinant in preserving volume when registering two images has been widely exploited in the past[24,25,38] and this volume-preserving regularization term could reduce the volume change in the total mass between source and target images. In this application, however, due to the constrained region of interest we opt for a different approach to preserve the volume of the coronary artery tree explicitly so that the volume of soft mask J remains constant while the flow is minimized using the projection technique.[39]

Let us first compute the variation in

$$E(h(x))=\int_{\Omega}m_I(x)|I(x)-J(h(x))|^2dx+\alpha\int_{\Omega}|\nabla h(x)|^2dx. \quad (7)$$

The derivative of $E(h(x))$ can be computed as follows: We take a path $h_t=h+t\tilde{h}$ of functions and take derivative with respect to t, and set $t=0$. We then get

$$\frac{d}{dt}E(h_t)|_{t=0} = \frac{d}{dt}\left(\int_\Omega m_I|I(x)-J(h_t)|^2 + \alpha\int_\Omega |\nabla h_t|^2 dx\right)$$
$$= 2\int_\Omega m_I(I(x)-J(h))(-J'_h(\tilde{h}))dx$$
$$+ 2\alpha\int_\Omega \nabla h\cdot\nabla\tilde{h}dx$$
$$= -2\int_\Omega m_I(I(x)-J(h))J'_h(\tilde{h})dx$$
$$+ 2\alpha\int_{\partial\Omega}\tilde{h}(\nabla h\cdot\vec{n})ds - 2\alpha\int_\Omega \tilde{h}\Delta h dx, \quad (8)$$

where $\vec{n}$ is unit outer normal vector of Ω and this can be viewed as $E'_h(\tilde{h})$, i.e., the derivative of E at h applying to $\tilde{h}$.

We then get

$$\nabla E(h(x)) = -2\int_\Omega m_I(x)(I(x)-J\circ h(x))\,\nabla J\circ h(x)dx$$
$$-2\alpha\int_\Omega \Delta h(x)dx,$$

$$\text{Boundary condition: } \nabla h\cdot\vec{n} = \frac{\partial h}{\partial n} = 0 \quad \text{on} \quad \partial\Omega. \quad (9)$$

We then construct a flow that minimizes E and also preserves the volume of $m_J\circ h(x)$,

$$V(h) = \int_\Omega m_J(h(x))dx. \quad (10)$$

The gradient of V is given by

$$\nabla V(h) = \nabla m_J\circ h(x). \quad (11)$$

The flow that preserves volume and minimizes E becomes

$$-\nabla E + \lambda\nabla V, \quad (12)$$

where we choose λ so that

$$(-\nabla E + \lambda\nabla V)dV(h) = 0 \quad (13)$$

because the volume does not change. Therefore, we get

$$\int_\Omega (-\nabla E + \lambda\nabla V)\nabla V dx = 0. \quad (14)$$

By solving Eq. (14) for λ, we have

$$\lambda = \frac{\int_\Omega \nabla E\nabla V dx}{\int_\Omega \nabla V\nabla V dx}$$
$$= -\frac{\int_\Omega [2m_I(I-J\circ h)\nabla J\circ h + 2\alpha\Delta h]\nabla m_J\circ h dx}{\int_\Omega |\nabla m_J(h(x))|^2 dx}. \quad (15)$$

This derivation is based on the projection technique that imposes a condition that the total flow in Eq. (12) should be orthogonal to the volume flow in Eq. (11) for preserving the volume. Volume constraint parameter λ is calculated iteratively according to Eq. (15) while the energy is minimized.

II.A.5. Minimization

Given the initialization of global displacement, we can find the optimal transformation by minimizing the flow associated with data fidelity, smoothness, and the volume-preserving constraint. The Euler–Lagrange equation, associated with flow that minimizes E and preserves volume V, is given by

$$h_{t+1} = h_t + \delta t(-\nabla E(h_t) + \lambda\nabla V(h_t))$$
$$= h_t + \delta t(2m_I(I-J\circ h_t)\nabla J\circ h_t + \alpha\Delta h_t + \lambda\nabla m_J\circ h_t), \quad (16)$$

where δt is the time step, t is the time index, λ is given in Eq. (15) and is found in an alternating manner, and α is a weighting parameter that defines the trade-off between the alignment of the two volumes and the smoothness of the transformation. We found experimentally that $\alpha=0.1$ provides a good compromise between the two terms.

For the computational efficiency, the global displacement is computed using an iterative multiresolution technique. In the subsequent stage, the energy functional of the local deformation is minimized numerically using the iterative gradient descent technique.[40] The algorithm stops if a local minimum of the energy functional is found or the number of iterations reaches a predefined limit of 200.

II.A.6. Implementation

The proposed coregistration algorithm is fully automatic and the global displacement model and subsequent local deformation model as described above are implemented using rigid coregistration in ITK (Insight Segmentation and registration Toolkit).[41] In addition, we used publicly available implementation[42] of dense nonparametric MI-based nonlinear coregistration and ITK (Ref. 41) implementation of *demons* algorithm[43] for the comparison with the proposed method.

We employed a multiresolution scheme for our global displacement model. The coregistration parameters are first estimated at the coarsest level, and these are then used as the starting parameters for the next level. Transformations at each level of the pyramid are accumulated and propagated, thus generating a single final transformation. The multiresolution scheme helps avoid local minima while achieving computational efficiency and robustness. In our implementation, we used 2 levels.

II.B. Experimental validation

II.B.1. Clinical data

Ten paired CCTA scans (20 scans in total) from ten patients were evaluated in this retrospective analysis. The imaging protocol has previously been described in detail by Dey *et al.*[44] Briefly, all CCTA scans were obtained with the same 64-slice dual source CT (DSCT) scanner (Definition; Siemens Medical Solutions, Forchheim, Germany) with a

TABLE I. Patient characteristics and image parameters of baseline and follow-up scans.

Patient No.	1	2	3	4	5	6	7	8	9	10
Gender	Male	Male	Male	Female	Male	Male	Female	Male	Male	Male
Age	79	64	82	79	50	60	85	52	59	62
Time difference (months)	4	15	11	5	15	10	15	19	12	1
Matrix size baseline	512×512×417	512×512×306	512×512×684	512×512×591	512×512×580	512×512×580	512×512×580	512×512×580	512×512×461	512×512×472
Matrix size follow-up	512×512×406	512×512×404	512×512×404	512×512×584	512×512×600	512×512×580	512×512×580	512×512×580	512×512×402	512×512×447
Pixel size baseline (mm)	0.43×0.43×0.3	0.39×0.39×0.4	0.4×0.4×0.29	0.36×0.36×0.3	0.39×0.39×0.3	0.39×0.39×0.3	0.39×0.39×0.3	0.39×0.39×0.3	0.31×0.31×0.3	0.35×0.35×0.3
Pixel size follow-up (mm)	0.47×0.47×0.3	0.45×0.45×0.3	0.45×0.45×0.3	0.36×0.36×0.3	0.39×0.39×0.3	0.39×0.39×0.3	0.39×0.39×0.3	0.39×0.39×0.3	0.34×0.34×0.3	0.36×0.36×0.3
Cardiac phase baseline/follow-up	70%/80%	70%/70%	70%/70%	65%/65%	65%/65%	70%/65%	65%/65%	70%/70%	65%/70%	65%/70%
Calcium score of baseline	178	205	148	0	27	Not available	123	801	54	148
Image quality of baseline	Good	Good	Excellent	Excellent	Good	Excellent	Good	Good	Good	Excellent
Image quality of follow-up	Good	Good	Excellent	Excellent	Excellent	Excellent	Good	Good	Excellent	Excellent
Estimated maximal stenosis severity of baseline	25%–49%	25%–49%	25%–49%	0%	1%–24%	50%–69%	1%–24%	70%–89%	50%–69%	25%–49%
Estimated maximal stenosis severity of follow-up	25%–49%	50%–69%	>90%	0%	1%–24%	>90%	1%–24%	25%–49%	1%–24%	25%–49%
Plaque type a t maximal stenosis baseline/ follow-up	Mixed/ mixed	Mixed/ mixed	Mixed/ noncalcified	0/0	Calcified/ noncalcified	Mixed/ mixed	Calcified/ calcified	Calcified/ calcified	Noncalcified/ mixed	Mixed/ mixed

890

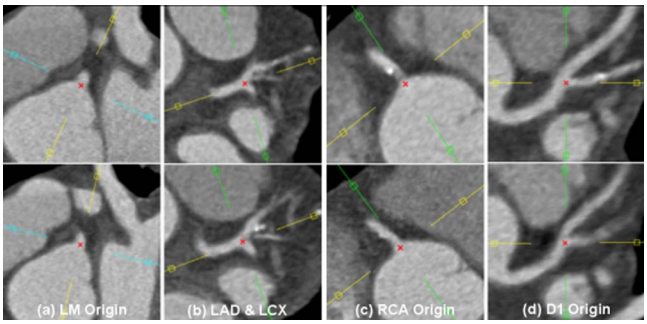

FIG. 3. Anatomical landmarks used for validation shown in one example case with images from a baseline scan at the top row and images from a follow-up scan at the bottom row. We have obtained independent sets of anatomical landmarks from two clinical observers. Crosses indicate the positions of landmarks, including the left main coronary artery origin (a), bifurcation of left anterior descending and left circumflex arteries (b), right coronary artery origin (c), and branch point of the first diagonal artery from the left anterior descending artery (d).

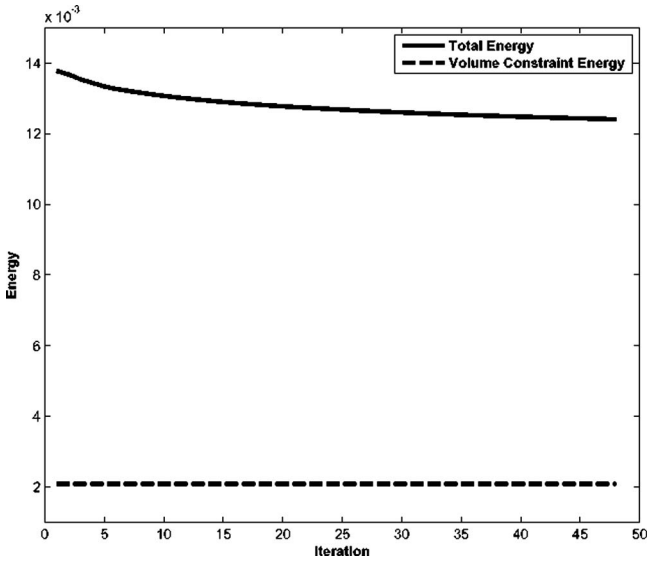

FIG. 4. Plot of the total energy and the energy under the volume-preserving constraint. For the latter, we preserve the volume of the coronary tree explicitly in such a way that the volume of soft mask J remains constant, while the flow is minimized. The energy of volume-preserving constraint is almost the same, while the total energy is minimized.

gantry-rotation time of 330 ms and a standard detector collimation of 0.6 mm. 80 ml of intravenous contrast was administered before each scan. Raw data were reconstructed using 0.6 mm slice thickness, 0.3 mm slice increment, a 250×250 mm^2 field of view, a transverse field of view encompassing the whole heart (with z-axis heart dimensions ranging from 159 to 241 mm in the tested datasets), single-segment reconstruction, and a medium-smooth reconstruction kernel (B26f). The time difference between baseline and follow-up scans ranged from 1 to 19 months. Patient characteristics and image parameters are described in Table I. The best phase of the cardiac cycle for the visualization of coronary arteries ranged from 65% to 80% of the R-R interval, as determined by an expert reader at the time of clinical assessment. The study was conducted according to the guidelines of the Cedars-Sinai Medical Center Institutional Review Board, and all patients gave written informed consent prior to use of their data.

II.B.2. Evaluation of automatic coregistration

We compared the results obtained with our proposed method to the dense nonparametric MI-based coregistration with diffusion regularization and to the demons algorithm[43] with and without histogram matching. In our experiment, for the MI-based coregistration we set the number of histograms bins to 10 and the number of sample size to 10% of the total number of voxels. We found the parameters that produce best results heuristically. The algorithm stops when the local minimum is found or the number of iterations reaches the predefined limit of 200 for all methods.

To assess the accuracy of the coregistration algorithm quantitatively, we calculated the target registration error (TRE), as defined by Fitzpatrick *et al.*,[45] which is the distance between a certain point in the target volume and the corresponding point in the source volume after coregistration, and can be described as

$$\mathrm{TRE}(r)=\frac{1}{m}\sum_{i=1}^{m}D(p_t^i(r),p_s^i(T\cdot r)), \tag{17}$$

where $p_t(r)$ and $p_s(T\cdot r)$ indicate the coordinates of the landmark point from target volume and the coordinate of the corresponding registered point from the source volume, respectively. D indicates the Euclidean distance between two points, and m denotes the number of points used for evaluations. Two expert observers independently selected several corresponding anatomical landmarks from each scan, and we calculated the mean and standard deviation of the pairwise distances of these landmarks after coregistration. We obtained several 3D landmarks at specific anatomical locations from each scan. These locations included the following anatomical locations: Left main (LM) artery origin, bifurcation of the left anterior descending (LAD), and left circumflex (LCX) arteries, right coronary artery (RCA) origin and branch point of the first diagonal (D1) from the LAD. Examples of those selected landmarks for one case are presented in Fig. 3. In addition, the alignment of serial scans was visually assessed qualitatively with the use of the "roving window" technique, where with a moving window one could interactively "rove" and reveal the registered image at the same position.

III. RESULTS

Serial CCTA coregistrations were performed on an Intel Core2 Duo CPU with a clock speed of 2.5 GHz and 4 Gbyte memory. The mean computation time for the whole process (both global displacement and local deformation) was 5.2 ± 0.5 min. The mean computation times for MI-based method and demons algorithm were 5.3 ± 0.5 and 4.4 ± 0.1 min, respectively. Our proposed method, MI-based

TABLE II. TRE comparison with different coregistration methods (Mean ± SD).

TRE (mm)	LM artery origin	Bifurcation of LM and LCX	RCA origin	Bifurcation of LAD and D1	Average
Before coregistration	49.51 ± 41.71	49.9 ± 41.01	50.54 ± 40.53	49.64 ± 41.42	**49.51 ± 41.71**
Global displacement	2.40 ± 1.10	1.88 ± 1.02	2.73 ± 1.53	1.89 ± 0.65	**2.22 ± 1.15** [a]
MI-based method after Global displacement	1.93 ± 0.89	1.46 ± 0.84	2.36 ± 1.53	1.57 ± 0.58	**1.83 ± 1.06** [a]
Demons method after Global displacement	1.97 ± 0.82	1.41 ± 1.13	2.44 ± 1.16	1.55 ± 0.45	**1.84 ± 1.00** [a]
Demons method after histogram matching	1.85 ± 0.63	1.38 ± 0.71	1.87 ± 1.39	1.52 ± 0.53	**1.66 ± 0.83** [a]
Proposed method without volume constraint	1.67 ± 0.65	1.24 ± 0.68	1.96 ± 1.13	1.54 ± 0.43	**1.60 ± 0.79**
Proposed method without mask	1.95 ± 0.89	1.44 ± 1.12	2.23 ± 1.23	1.52 ± 0.47	**1.78 ± 1.00** [a]
Proposed method	1.65 ± 0.59	1.21 ± 0.68	1.75 ± 1.02	1.64 ± 0.51	**1.56 ± 0.74**

[a] $p < 0.05$ vs proposed method.

method, and demons algorithm achieved a success rate of 90% as assessed visually (1 failed out of 10 datasets). The failed case had an error of 5.4 mm. In this patient, there was no change in the coronary arteries, which were assessed to be normal. However, there was severe aneurysmal dilation of the aortic root and the ascending aorta which caused a significant change. We have therefore excluded the failed case in the following results.

In Fig. 4, we present graphs of the average total energy and the average energy derived by the volume preserving for five consecutive cases as a function of the number of iterations.

In Table II, we presented the TRE comparison of original distance before coregistration, global displacement, and local deformation. In addition, we performed experiments without using the soft mask or volume constraint and with the MI-based method and with demons algorithm.[43] We also applied the demons algorithm with and without histogram matching. To obtain these measurements, we considered each anatomical landmark as a 3D point and then transformed it using each of the coregistration methods. In all cases the original data misalignments were larger than 40 mm. Our proposed method resulted in mean TRE of global displacement was 2.22 ± 1.15 mm and further improved to 1.56 ± 0.74 mm with subsequent local deformation ($p < 0.05$) compared to 1.83 ± 1.06, 1.84 ± 1.00, and 1.66 ± 0.83 mm for MI-based coregistration and demons algorithm with and without histogram matching, respectively ($p < 0.05$). There was a trend for the proposed method toward better accuracy compared to the same methods without using soft mask, but it did not reach the statistical significance ($p = 0.1896$). The importance of local deformations is shown in Fig. 5, where images with only global displacement correction and with additional local deformation correction are presented. Although global displacement coregistration using a presegmented mask performed well in terms of TRE, we still observed misalignment when visually comparing source and target images in Fig. 5. This visual misalignment was significantly reduced with local deformation correction.

In addition, since we did not impose the symmetric consistency constraint,[23,46] which guarantees that the estimated forward transformation (source to target) equals that of inverse transformation (target to source) due to computational efficiency, we performed inverse consistency experiments using the landmarks obtained. To show the inverse consistency error, registered landmarks obtained using forward transformation (source to target) were transformed using inverse mapping by replacing the source and target volumes. We then calculated inverse target registration errors between source landmarks and the inversely registered points. As shown in Table III, the error was less than the voxel size of 0.15 mm.

We also calculated the distances between two observers for 100 landmark points (5 landmarks for each of 20 scans) to measure the interobserver variability of the reference standard. Table IV shows the observer variability. For qualitative assessments of image coregistration, the roving window technique was utilized, as shown in Fig. 6.

In Figs. 7 and 8, we show two examples of the final coregistration results for a case with observed change and for a case without observed changes in the plaque lesion, respec-

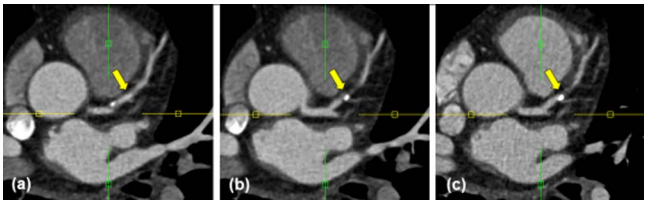

FIG. 5. Example of global displacement and local deformation techniques. Global displacement model (a) resulted in 2.0 mm for TRE and subsequently local deformation (b) improved this result to 1.4 mm for TRE. The target image is shown in (c). The lesion is marked with arrows. The global displacement model performs similarly to the local deformation model in terms of quantitative measurements, but visual assessment in specific cases showed there is still error especially in small plaque areas.

TABLE III. Inverse consistency error.

Inverse consistency error	Mean ± SD (mm)
LM artery origin	0.13 ± 0.02
Bifurcation of LM and LCX	0.14 ± 0.04
RCA origin	0.12 ± 0.10
Bifurcation of LAD and D1	0.17 ± 0.06
Average	**0.14 ± 0.06**

TABLE IV. Average landmark distances between two observers for each landmark ($n=100$).

Observer variability	Mean ± SD (mm)	Max (mm)	Min (mm)
LM artery origin	1.20 ± 0.41	1.80	0.41
Bifurcation of LM and LCX	1.30 ± 0.67	2.31	0.63
RCA origin	1.33 ± 0.54	2.12	0.42
Bifurcation of LAD and D1	1.42 ± 0.75	2.45	0.44
Average	**1.31 ± 0.91**	**2.42**	**0.41**

tively. In Fig. 7, the images show significant plaque progression in the proximal LAD, where luminal diameter stenosis from mixed plaque increased from approximately 45% to ≥90%, as visually assessed by an expert reader. In Fig. 8, images from the baseline and follow-up CCTA show no significant change in the proximal calcified plaque, which appeared to cause an estimated 25%–49% stenosis in both studies. These visual comparisons can be made easily on coregistered images.

IV. DISCUSSION

In this study, we proposed and evaluated a fully automated method to register serial CCTA scans for plaque evaluation. Although there have been some other studies that measure shape/volume changes or longitudinal changes[26–29] with different modalities, to the best of our knowledge, this is the first report of image registration techniques applied to the measurement of longitudinal changes in CCTA. We have demonstrated that our two-step coregistration using a feature mask is an effective approach for monitoring plaque progression or regression obtained from serial high-resolution CCTA scans. A global displacement model was used to find the global transformation based on the segmented coronary tree structures from CCTA scans. This initial registration using the segmented coronary tree is crucial in this application since original data misalignments were larger than 40 mm, and thus localization of small regions of interest is important. For instance, we performed rigid registration using whole volumes (without using the segmented coronary tree) and achieved results worse than original data misalignment (>40 mm). Subsequently, nonlinear transformation using a local deformation model was performed to find optimal local deformations, where a 3D feature mask (soft mask) was introduced as a weighting function approximating the coronary vessel and surrounding region. The mask was also utilized for a volume-preserving constraint. The proposed method was validated on ten paired CCTA datasets (20 scans in total) obtained on a dual source CT scanner. Robust and accurate target registration error was obtained with respect to the ground truth, as visually determined by two expert CCTA readers. The overall coregistration errors were 2.22 ± 1.15 mm for global displacement and 1.56 ± 0.74 mm after further local deformation. In comparison, the interobserver variability was 1.31 ± 0.91 mm. In addition, we measured the inverse consistency error of coreg-

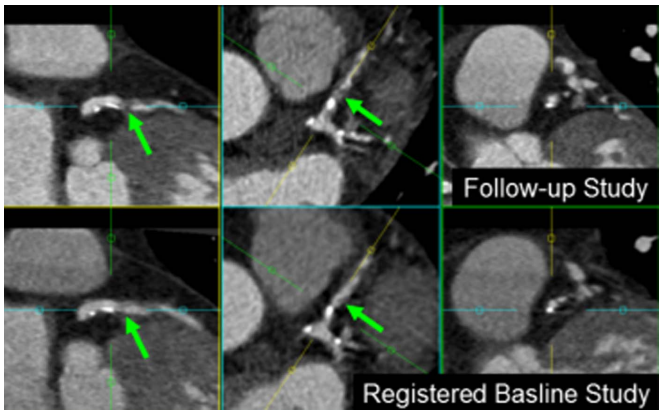

FIG. 7. Clinical example of plaque lesion progression (worsening) in an 82-year old man. The top row shows a follow-up study and bottom row shows a registered baseline study. The time difference between the two scans was 11 months. The pixel sizes of baseline and follow-up study were $0.4\times0.4\times0.29$ mm and $0.45\times0.45\times0.3$ mm, respectively. Arrows show increased, noncalcified plaque and stenosis in follow-up study.

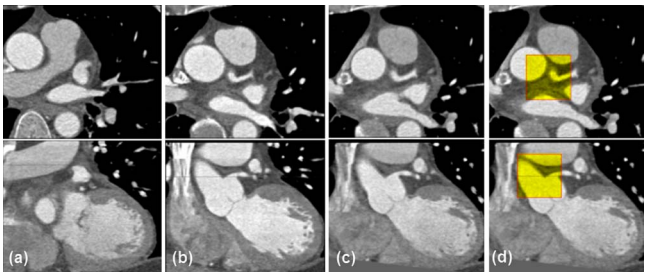

FIG. 6. Example of coregistration results. Baseline image is registered to the follow-up image. Transverse orientation is shown at the top row, and coronal orientation is shown at the bottom row. The original baseline image before (a) and after (b) coregistration is shown. Panel (c) shows the follow-up image. As shown in (a), the original image is significantly misaligned. The "roving window" technique in (d) using a portion of the registered image from (b) to the target image in (c) shows that the result from our method is visually accurate.

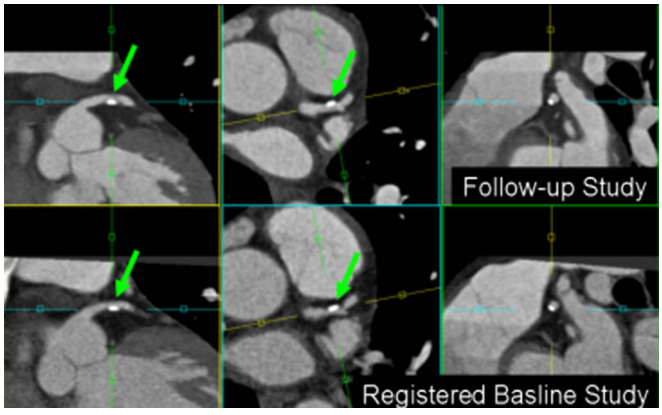

FIG. 8. Clinical example of plaque without significant changes in a 59-year old man. Top row shows the follow-up study and the bottom row shows the registered baseline study. The lesion is marked with arrows. The time difference between the two scans was 12 months. The pixel sizes of baseline and follow-up study were $0.31\times0.31\times0.3$ mm and $0.34\times0.34\times0.3$ mm, respectively.

istration by switching source and target scans and obtained average errors of 0.14 ± 0.06 mm. Coregistration of the patient data achieved 90% success rate by visual confirmation.

The sum of squared differences (L^2-norm) was used as the similarity measure since serial scans from the same modality were being considered. Note that, in general, the SSD measure has been widely used for serial MR coregistration[47,48] and CT registration.[49–51] The problem of potential differences in image intensities was addressed by the use of histogram matching, ensuring that corresponding points in different volumes have similar intensity values for the nonlinear registration step. The energy functional of the proposed coregistration algorithm is dependent on both an intensity-based data term and a shape-based term which can compensate for the limitations of using the SSD measure, thus producing robust and accurate results. MI-based measures may appear appealing for this application since the intensities of corresponding voxels may differ between the images; however, we performed additional experiments using dense nonparametric MI-based coregistration and obtained inferior results (1.83 ± 1.06 mm) compared to the proposed method (1.56 ± 0.74 mm). We also measured the mean TRE without using the volume-preserving constraint and found it not to be significantly different ($p=0.1342$). However, volume-preserving constraint must be utilized in order to ensure correct depiction of plaque lesions on both scans. This is partly because target plaque area is very small (2–3 mm) and interobserver variability is high. We measured the mean TRE with demons method after histogram matching (1.66 ± 0.83 mm) and found it to be slightly higher than that of the proposed method (1.56 ± 0.74 mm).

Serial coregistration in the context of this application is challenging since the region of interest (coronary arteries) is small, coronary plaque size is small compared to CT spatial resolution, and CCTA scans are acquired at two separate times with variations in coverage, contrast intensity level, cardiac phase selected for optimal reconstruction, and different imaging artifacts. In addition, because of potential progression in coronary plaque, topological equivalence between baseline and follow-up scans may be violated but volume needs to be preserved. To our knowledge, these challenges have not been previously studied for this application. To address these challenges, we exploited the binary mask obtained from presegmented coronary trees to further guide coregistration. However, this segmented feature-based approach will admittedly affect the coregistration accuracy if the coronary tree segmentation is incorrect. Therefore, a Gaussian kernel was applied to weaken the bias of segmentation in the local deformation model. We observed that visual assessment of our method showed accurate coregistration of serial volumetric CCTA scans with one case failing due to severe aneurysmal dilation of the ascending aorta.

It has been reported previously that the mean increase in noncalcified plaque volume measured from CCTA was 22% for the left main coronary artery.[6] A recent study[52] from our group reported mean measured plaque lengths of 10.5 ± 6.2 mm in the proximal segments of the coronary arteries. The TRE after our proposed registration was 1.56 ± 0.74 mm and if we consider proximal plaques with lengths similar to our reported study, this error is approximately 15% of the plaque length. However, note that even though visual assessment showed accurate registration, the interobserver variability in landmark positions, used to determine TRE, was 1.31 ± 0.91 mm. Therefore, it is most likely that the TRE is exaggerated by the observer variability.

Our approach has several potential limitations. Quantitative evaluation of the coregistration is challenging since there is no true gold standard other than visual judgment, which is associated with interobserver variability. To account for this, we measured target registration error using representative anatomical landmarks. Though this could provide a quantitative measure of the error, it is still subject to variability between human observers. In addition, plaque lesions can change between the two time points due to physiological processes, thereby taking away any direct point to point correspondence in image intensities. In our variational framework, the applied diffusion regularization may not be well-suited for the phenomena of plaque development, resulting in distortion at the vicinity of the plaque boundary. However, our volume-preserving term uses an anatomical feature mask to explicitly constrain the volume change in the source image. Since the objective of serial registration is to align plaque located in the artery without any artificial bending or deformation, we constrain the volume of the coronary artery of the source image. This allows one to measure and monitor the progression or regression of the plaque regions. To deemphasize the strong bias of the binary mask obtained from segmenting the coronary lumen, we applied Gaussian kernel to the binary luminal mask.

Serial CCTA is clinically attractive because it holds promise for assessing changes in coronary artery plaque burden and response to therapy. With improvement in multidetector CT technology and reduction in associated radiation dose, we expect efforts for improved assessment of change in coronary plaque to significantly increase in the near future. Rapid and effective CCTA coregistration can help facilitate improved the evaluation of plaque change.

V. CONCLUSIONS

We have developed a novel, fully automatic nonlinear feature-based volume coregistration algorithm for serial CCTA scans. We incorporated segmented coronary tree structures as anatomical and geometric features for the coregistration that helps localize the structure of interest. Our proposed feature-based method provides accurate and robust coregistration with accuracy of 1.56 mm and 90% success rate as tested in datasets from ten paired scans. Our results demonstrated the feasibility of the proposed coregistration algorithm for the analysis of serial plaque changes.

ACKNOWLEDGMENTS

This study was supported by AHA Award No. 09GRNT2330000 (PI: Damini Dey), and by Grant No. 6318

from the Glazer Foundation, and a grant from the Lincy Foundation, Los Angeles, CA.

[a]Electronic mail: piotr.slomka@cshs.org

[1]S. Achenbach, "Cardiac CT: State of the art for the detection of coronary arterial stenosis," J. Cardiovasc. Comput. Tomogr. **1**(1), 3–20 (2007).
[2]D. S. Berman, L. J. Shaw, R. Hachamovitch, J. D. Friedman, D. M. Polk, S. W. Hayes, L. E. J. Thomson, G. Germano, N. D. Wong, K. Xingping, and A. Rozanski, "Comparative use of radionuclide stress testing, coronary artery calcium scanning, and noninvasive coronary angiography for diagnostic and prognostic cardiac assessment," Semin Nucl. Med. **37**, 2–16 (2007).
[3]A. W. Leber, A. Becker, A. Knez, F. Von Ziegler, M. Sirol, K. Nikolaou, B. Ohnesorge, Z. A. Fayad, C. R. Becker, M. Reiser, G. Steinbeck, and P. Boekstegers, "Accuracy of 64-slice computed tomography to classify and quantify plaque volumes in the proximal coronary system: A comparative study using intravascular ultrasound," J. Am. Coll. Cardiol. **47**, 672–677 (2006).
[4]A. W. Leber, A. Knez, A. Becker, C. Becker, F. von Ziegler, K. Nikolaou, C. Rist, M. Reiser, C. White, G. Steinbeck, and P. Boekstegers, "Accuracy of multidetector spiral computed tomography in identifying and differentiating the composition of coronary atherosclerotic plaques: A comparative study with intracoronary ultrasound," J. Am. Coll. Cardiol. **43**, 1241–1247 (2004).
[5]S. Achenbach, D. Ropers, U. Hoffmann, B. MacNeill, U. Baum, K. Pohle, T. Brady, E. Pomerantsev, J. Ludwig, F. Flachskampf, S. Wicky, I. Jang, and W. Daniel, "Assessment of coronary remodeling in stenotic and nonstenotic coronary atherosclerotic lesions by multidetector spiral computed tomography," J. Am. Coll. Cardiol. **43**, 842–847 (2004).
[6]M. Schmid, S. Achenbach, D. Ropers, S. Komatsu, U. Ropers, W. G. Daniel, and T. Pflederer, "Assessment of changes in non-calcified atherosclerotic plaque volume in the left main and left anterior descending coronary arteries over time by 64-slice computed tomography," Am. J. Cardiol. **101**, 579–584 (2008).
[7]C. Burgstahler, A. Reimann, T. Beck, A. Kuettner, D. Baumann, M. Heuschmid, H. Brodoefel, C. D. Claussen, A. F. Kopp, and S. Schroeder, "Influence of a lipid-lowering therapy on calcified and noncalcified coronary plaques monitored by multislice detector computed tomography: Results of the New Age II pilot study," Invest. Radiol. **42**, 189–195 (2007).
[8]M. Ferencik, D. Ropers, S. Abbara, R. C. Cury, U. Hoffmann, K. Nieman, T. J. Brady, F. Moselewski, W. G. Daniel, and S. Achenbach, "Diagnostic accuracy of image postprocessing methods for the detection of coronary artery stenoses by using multidetector CT," Radiology **243**, 696–702 (2007).
[9]S. Achenbach, "Computed tomography coronary angiography," J. Am. Coll. Cardiol. **48**, 1919–1928 (2006).
[10]S. Sola and M. Y. Desai, "Measuring coronary artery plaque volume and composition by MDCT: Too much, too soon?," Journal of Cardiovascular Computed Tomography **3**(5), 321–322 (2009).
[11]V. Y. Cheng, R. Nakazato, D. Dey, S. Gurudevan, J. Tabak, M. J. Budoff, R. P. Karlsberg, J. Min, and D. S. Berman, "Reproducibility of coronary artery plaque volume and composition quantification by 64-detector row coronary computed tomographic angiography: An intraobserver, interobserver, and interscan variability study," J. Cardiovasc. Comput. Tomogr. **3**(5), 312–320 (2009).
[12]T. Makela, P. Clarysse, O. Sipila, N. Pauna, Q. C. Pham, T. Katila, and I. E. Magnin, "A review of cardiac image registration methods," IEEE Trans. Med. Imaging **21**, 1011–1021 (2002).
[13]C. K. Hoh, M. Dahlbom, G. Harris, Y. Choi, R. A. Hawkins, M. E. Phelps, and J. Maddahi, "Automated iterative three-dimensional registration of positron emission tomography images," J. Nucl. Med. **34**, 2009–2018 (1993).
[14]D. Collins, T. Peters, and A. Evans, "Automated 3D nonlinear deformation procedure for determination of gross morphometric variability in human brain," Proc. SPIE **2359**, 180–190 (1994).
[15]P. J. Slomka, J. Mandel, D. Downey, and A. Fenster, "Evaluation of voxel-based registration of 3-D power Doppler ultrasound and 3-D magnetic resonance angiographic images of carotid arteries," Ultrasound Med. Biol. **27**, 945–955 (2001).
[16]M. Holden, "A review of geometric transformations for nonrigid body registration," IEEE Trans. Med. Imaging **27**, 111–128 (2008).
[17]W. M. Wells, P. Viola, H. Atsumi, S. Nakajima, and R. Kikinis, "Multi-modal volume registration by maximization of mutual information," Med. Image Anal. **1**(1), 35–51 (1996).
[18]B. Fischer and J. Modersitzki, "Curvature based image registration," J. Math. Imaging Vision **18**, 81–85 (2003).
[19]B. Fischer and J. Modersitzki, "A unified approach to fast image registration and a new curvature based registration technique," Linear Algebr. Appl. **380**, 107–124 (2004).
[20]B. Fischer and J. Modersitzki, "Fast diffusion registration," AMS Contemporary Mathematics, Inverse Problems, Image Analysis, and Medical Imaging **313**, 117–129 (2002).
[21]H. Lester and S. R. Arridge, "A survey of hierarchical non-linear medical image registration," Pattern Recogn. **32**, 129–149 (1999).
[22]E. D'Agostino, F. Maes, D. Vandermeulen, and P. Suetens, "A viscous fluid model for multimodal non-rigid image registration using mutual information," Med. Image Anal. **7**, 565–575 (2003).
[23]G. E. Christensen and H. J. Johnson, "Consistent image registration," IEEE Trans. Med. Imaging **20**, 568–582 (2001).
[24]T. Rohlfing, C. R. Maurer, Jr., D. A. Bluemke, and M. A. Jacobs, "Volume-preserving nonrigid registration of MR breast images using free-form deformation with an incompressibility constraint," IEEE Trans. Med. Imaging **22**, 730–741 (2003).
[25]E. Haber and J. Modersitzki, "Numerical methods for volume preserving image registration," Inverse Probl. **20**, 1621–1638 (2004).
[26]W. R. Crum, R. I. Scahill, and N. C. Fox, "Automated hippocampal segmentation by regional fluid registration of serial MRI: Validation and application in Alzheimer's disease," Neuroimage **13**, 847–855 (2001).
[27]D. Rey, G. Subsol, H. Delingette, and N. Ayache, "Automatic detection and segmentation of evolving processes in 3D medical images: Application to multiple sclerosis," Med. Image Anal. **6**, 163–179 (2002).
[28]K. K. Leung, M. Holden, N. Saeed, K. J. Brooks, J. B. Buckton, A. A. Williams, S. P. Campbell, K. Changani, D. G. Reid, Y. Zhao, M. Wilde, D. Rueckert, J. V. Hajnal, and D. L. Hill, "Automatic quantification of changes in bone in serial MR images of joints," IEEE Trans. Med. Imaging **25**, 1617–1626 (2006).
[29]T. Hartkens, D. L. Hill, A. D. Castellano-Smith, D. J. Hawkes, C. R. Maurer, Jr., A. J. Martin, W. A. Hall, H. Liu, and C. L. Truwit, "Measurement and analysis of brain deformation during neurosurgery," IEEE Trans. Med. Imaging **22**, 82–92 (2003).
[30]H. Wang, L. Dong, J. O'Daniel, R. Mohan, A. S. Garden, K. K. Ang, D. A. Kuban, M. Bonnen, J. Y. Chang, and R. Cheung, "Validation of an accelerated 'demons' algorithm for deformable image registration in radiation therapy," Phys. Med. Biol. **50**, 2887–2905 (2005).
[31]P. J. Slomka and R. P. Baum, "Multimodality image registration with software: State-of-the-art," Eur. J. Nucl. Med. Mol. Imaging **36** Suppl 1, 44–55 (2008).
[32]J. Shi, B. Sahiner, H. P. Chan, L. Hadjiiski, C. Zhou, P. N. Cascade, N. Bogot, E. A. Kazerooni, Y. T. Wu, and J. Wei, "Pulmonary nodule registration in serial CT scans based on rib anatomy and nodule template matching," Med. Phys. **34**, 1336–1347 (2007).
[33]T. R. Mackie, J. Kapatoes, K. Ruchala, W. Lu, C. Wu, G. Olivera, L. Forrest, W. Tome, J. Welsh, R. Jeraj, P. Harari, P. Reckwerdt, B. Paliwal, M. Ritter, H. Keller, J. Fowler, and M. Mehta, "Image guidance for precise conformal radiotherapy," Int. J. Radiat. Oncol., Biol., Phys. **56**, 89–105 (2003).
[34]H. Takao, I. Doi, and M. Tateno, "Evaluation of an automated system for temporal subtraction of thin-section thoracic CT," Br. J. Radiol. **80**, 85–89 (2007).
[35]J. Woo, B.-W. Hong, D. Dey, G. Sundaramoorthi, A. Ramesh, G. Germano, V. Cheng, C.-C. Jay Kuo, and P. Slomka, "Feature-based non-rigid volume registration of serial coronary CT angiography," Proc. SPIE Symposium on Medical Imaging, Vol. 7259, Orlando, Florida, February 2009.
[36]A. Hennemutha, T. Boskampa, D. Fritzc, C. Kühnela, S. Bocka, D. Rinckb, M. Scheueringb, and H.-O. Peitgen, "One-click coronary tree segmentation in CT angiographic images," Computer Assisted Radiology and Surgery **1281**, 317–321 (2005).
[37]B. Horn and B. Schunck, "Determining optical flow," Artif. Intell. **17**, 185–203 (1981).
[38]P. J. Edwards, D. L. Hill, J. A. Little, and D. J. Hawkes, "A three-component deformation model for image-guided surgery," Med. Image Anal. **2**, 355–367 (1998).
[39]A. Yezzi, A. Tsai, and A. Willsky, "A fully global approach to image segmentation via coupled curve evolution equations," J. Visual Commun. Image Represent **13**, 195–216 (2002).

[40]J. Nocedal and S. J. Wright, *Numerical Optimization* (Springer-Verlag, New York, 1999).
[41]L. Ibanez, W. Schroeder, L. Ng, and J. Cates, *The ITK Software Guide*, 2nd edition (Kitware, Inc., Clifton Park, NY, 2005).
[42]M. De Craene, A. du Bois d'Aische, B. Macq, and S. Warfield, "Incorporating metric flows and sparse Jacobian transformations in ITK," The Insight Journal, URL http://hdl.handle.net/1926/183.
[43]J. P. Thirion, "Image matching as a diffusion process: An analogy with Maxwell's demons," Med. Image Anal. **2**, 243–260 (1998).
[44]D. Dey, C. J. Lee, M. Ohba, A. Gutstein, P. J. Slomka, V. Cheng, Y. Suzuki, S. Suzuki, A. Wolak, L. Le Meunier, L. E. J. Thomson, I. Cohen, J. D. Friedman, G. Germano, and D. S. Berman, "Image quality and artifacts in coronary CT angiography with dual-source CT: Initial clinical experience," J. Cardiovasc. Comput. Tomogr. **2**(2), 105–114 (2008).
[45]J. M. Fitzpatrick, J. B. West, and C. R. Maurer, Jr., "Predicting error in rigid-body point-based registration," IEEE Trans. Med. Imaging **17**, 694–702 (1998).
[46]A. Leow, S. C. Huang, A. Geng, J. Becker, S. Davis, A. Toga, and P. Thompson, "Inverse consistent mapping in 3D deformable image registration: Its construction and statistical properties," Inf. Process. Med. Imaging **19**, 493–503 (2005).
[47]J. V. Hajnal, N. Saeed, A. Oatridge, E. J. Williams, I. R. Young, and G. M. Bydder, "Detection of subtle brain changes using subvoxel registration and subtraction of serial MR images," J. Comput. Assist. Tomogr. **19**, 677–691 (1995).
[48]J. V. Hajnal, N. Saeed, E. J. Soar, A. Oatridge, I. R. Young, and G. M. Bydder, "A registration and interpolation procedure for subvoxel matching of serially acquired MR images," J. Comput. Assist. Tomogr. **19**(2), 289–296 (1995).
[49]B. Li, G. E. Christensen, E. A. Hoffman, G. McLennan, and J. M. Reinhardt, "Establishing a normative atlas of the human lung: Intersubject warping and registration of volumetric CT images," Acad. Radiol. **10**, 255–265 (2003).
[50]W. Lu, M. L. Chen, G. H. Olivera, K. J. Ruchala, and T. R. Mackie, "Fast free-form deformable registration via calculus of variations," Phys. Med. Biol. **49**, 3067–3087 (2004).
[51]D. Sarrut, V. Boldea, S. Miguet, and C. Ginestet, "Simulation of four-dimensional CT images from deformable registration between inhale and exhale breath-hold CT scans," Med. Phys. **33**, 605–617 (2006).
[52]L. Le Meunier, P. Slomka, D. Dey, V. Cheng, L. E. Thomson, S. Hayes, J. Friedman, G. Germano, and D. Berman, "Feasibility of coronary plaque imaging with FDG high-definition PET: Phantom study," Soc Nuclear Med **49**(1), 188 (2008) (Abstract).